



Cite this: *RSC Adv.*, 2023, **13**, 9811

## A coumarin-based fluorescent chemosensor as a Sn indicator and a fluorescent cellular imaging agent†

Hamide Hosseini-Jani-Pirdehi,<sup>a</sup> Soodeh Amigh,<sup>b</sup> Afshan Mohajeri,<sup>c</sup> Elahe Nazeri,<sup>a</sup> Amir Taheri,<sup>a</sup> Keivan Majidzadeh-A,<sup>a</sup> Zahra Mohammadpour<sup>b</sup> <sup>\*d</sup> and Rezvan Esmaeili <sup>\*a</sup>

In the present study, fluorogenic coumarin-based probes (**1–3**) through condensation of 4-hydroxy coumarin with malondialdehyde bis(diethyl acetal)/triethyl orthoformate were prepared. The absorption and fluorescence emission properties of **2b** and **3** in different solvents were studied, and a considerable solvatochromic effect was observed. The sensitivity of chemosensors **2b** and **3** toward various cations and anions was investigated. It was revealed that compound **3** had a distinct selectivity toward  $\text{Sn}^{2+}$ , possibly *via* a chelation enhanced quenching mechanism. The fluorescence signal was quenched over the concentration range of 6.6–120  $\mu\text{M}$ , with an LOD value of 3.89  $\mu\text{M}$ . The cytotoxicity evaluation of **3** against breast cancer cell lines demonstrated that the chemosensor was nontoxic and could be used successfully in cellular imaging. The probe responded to tin ions not only *via* fluorescence quenching, but also through colorimetric signal change. The change in optical properties was observed in ambient conditions and inside living cells.

Received 9th December 2022  
 Accepted 11th March 2023

DOI: 10.1039/d2ra07884h  
[rsc.li/rsc-advances](http://rsc.li/rsc-advances)

## 1 Introduction

Tin is a heavy metal with widespread use in industry. It is employed as a protective coating in the food industry for canned foods and drinks.<sup>1</sup> As fluoride or chloride salts, it is used in toothpaste, soap, perfume, and food additives. Furthermore, organotin compounds are applied in preparing plastics and pesticides.<sup>2</sup> Due to the widespread use of organic and inorganic tin compounds, large amounts of this ion discharge into aquatic systems and the environment, which pose serious health issues to various organisms and human lives at high concentrations. As a reducing agent,  $\text{SnCl}_2$  is necessary for fixation of technetium-99 (Tc-99m) radioisotope on pharmaceuticals. Tc-99m and  $\text{SnCl}_2$  are co-administered intravenously for diagnostic purposes in nuclear medicine. Reports indicated that  $\text{Sn}^{2+}$  could cause damage to DNA.<sup>3–6</sup> Moreover, Turgay Şişman observed teratogenic effects in zebrafish embryos after exposure to various concentrations of  $\text{SnCl}_2$ .<sup>7</sup> Therefore,

detecting tin ions in a selective and sensitive manner is essential.

Among the analytical techniques available for quantitatively measuring  $\text{Sn}^{2+}$  ions, only a few reports are devoted to electrochemical analyses.<sup>8–10</sup> Most studies have focused on molecular probes for colorimetric and fluorometric assay of Sn ions in both oxidation states (II and IV).<sup>11–20</sup> Fluorometric approaches offer rapid detection, the feasibility of operation, and high sensitivity. Their sensing mechanism is based on fluorescence enhancement or quenching in the presence of a target analyte. Coumarin-based fluorescent probes have received special attention for sensing various metal ions, including  $\text{Pb}^{2+}$ ,<sup>21</sup>  $\text{Hg}^{2+}$ ,<sup>22,23</sup> and  $\text{Cu}^{2+}$ ,<sup>24,25</sup> among others.<sup>26–28</sup> Coumarin, a natural compound found in plants, belongs to flavonoids and possesses a variety of biological activities. Its importance in biology relies on its antiviral, anti-inflammatory, anticancer, antioxidant, enzyme inhibition, and antimicrobial properties.<sup>29</sup> Alongside the biological features, coumarin is a fluorophore with high quantum yield and photostability, thus exhibiting promising performance in detecting metal ions at trace levels. Furthermore, its toxicity is low and other molecules can easily modify it for functionality enhancement. To this end, coumarin is linked to other molecules by several linkers including hydrazine,<sup>30,31</sup> ethylenediamine,<sup>32</sup> tris(2-aminoethyl) amine,<sup>33</sup> and diethylenetriamine.<sup>34</sup>

In the present study, we synthesized compound **3**, a derivative of coumarin, to detect  $\text{Sn}^{2+}$  ions in aqueous environments *via* fluorescence quenching selectively. We found that the synthesized compound was nontoxic to cells, ensuring their

<sup>a</sup>Genetics Department, Breast Cancer Research Center, Motamed Cancer Institute, ACECR, Tehran, Iran. E-mail: esmaeili.rezvan@gmail.com; r\_esmaeili@acecr.ac.ir

<sup>b</sup>Department of Chemistry, Shahid Bahonar University of Kerman, Kerman, Iran

<sup>c</sup>Department of Chemistry, College of Sciences, Shiraz University, Shiraz 7194684795, Iran

<sup>d</sup>Biomaterials and Tissue Engineering Department, Breast Cancer Research Center, Motamed Cancer Institute, ACECR, Tehran, Iran. E-mail: mohammadpour@acecr.ac.ir

† Electronic supplementary information (ESI) available. See DOI: <https://doi.org/10.1039/d2ra07884h>



biocompatibility. Therefore, we employed the synthesized compound for the imaging of  $\text{Sn}^{2+}$  in cellular models. The present research is an extension of our research on synthesizing chemosensors active in cellular environments.<sup>35</sup> Herein, we report the malondialdehyde bis(diethyl acetal)-based coumarin derivatives as fluorescent indicators, which among them only compound 3 demonstrated a high potency to  $\text{Sn}^{2+}$  detection.

## 2 Experiment section

### 2.1 Materials and instruments

All of the solvents and reagents were purchased from Merck and Sigma-Aldrich. Melting points were measured with an Electro-thermal 9100 apparatus without corrections. FTIR spectra were recorded on a NICOLET FTIR 100 spectrometer using KBr pellets. Ultraviolet-Visible (UV-Vis) and fluorescence spectra were recorded with a Rayleigh UV-2601 double-beam spectrophotometer and a PerkinElmer LS45 fluorescence spectrophotometer, respectively.  $^1\text{H}$  NMR and  $^{13}\text{C}$  NMR spectra were measured with Bruker DRX-500 AVANCE spectrometer. Chemical shifts of  $^1\text{H}$  and  $^{13}\text{C}$  NMR spectra were expressed in parts per million (ppm) downfield from tetramethylsilane (TMS) as an internal reference, using chloroform ( $\text{CDCl}_3$ ) and dimethyl sulfoxide ( $\text{DMSO-d}_6$ ) as the solvents at room temperature (25 °C). Mass spectra were recorded on a FINNIGAN-MATT 8430 mass spectrometer operating at an ionization potential of 20 or 70 eV. The CHN analysis was performed on a Vario ELIII elemental analyzer.

### 2.2 Synthesis of 3-(4-hydroxy-2-oxo-2*H*-chromen-3-ylmethylene)-chromane-2,4-dione (1)

4-Hydroxy coumarin (2.0 eq.,  $2.0 \times 10^{-3}$  mol, 0.324 g) and triethyl orthoformate (1.0 eq.,  $1.0 \times 10^{-3}$  mol, 0.148 g) were dissolved in dry acetonitrile ( $1.0 \times 10^{-3}$  L). The reaction mixture was allowed to stir at 70 °C for 3 hours. After completion of the reaction, monitored by TLC, the reaction mixture was filtered and the residue was washed with cold acetonitrile. A white powder was obtained in 80% yield (0.269 g). The ESI† extensively discusses the characterization data of compound 1 (Fig. A.1 and A.2†).

### 2.3 Synthesis of (3*Z*,3*Z*’)-3,3’-(propane-1,3-diylidene) bis(chromane-2,4-dione) (2a)

4-Hydroxy coumarin (2.0 eq.,  $2.0 \times 10^{-3}$  mol, 0.324 g) and malondialdehyde bis(diethyl acetal) (1.0 eq.,  $1.0 \times 10^{-3}$  mol, 0.22 g) were dissolved in dry acetonitrile ( $1.0 \times 10^{-3}$  L). The reaction mixture allowed to stir at 70 °C for 5 hours. After completion of the reaction, monitored by TLC, the reaction mixture was filtered, the residue was washed with cold acetonitrile. A white powder was obtained in 90% yield (0.324 g). The ESI† extensively discusses characterization data of compound 2a (Fig. B.1 and B.2†).

### 2.4 Synthesis of 3-[3-hydroxy-3-(4-hydroxy-2-oxo-2*H*-chromen-3-yl)-propylidene]-chromane-2, 4-dione (2b)

Compound 2a is a white powder, which upon dispersion in DMF or water, converts to 2b. The chemical transformation is irreversible. To this end, (0.0108 g,  $3.0 \times 10^{-5}$  mol) of 2a was dissolved in DMF ( $1.0 \times 10^{-2}$  L) to afford the stock solution with the concentration of  $3.0 \times 10^{-3}$  M. After 4 hours, the solution color changed to pink. This stock solution was diluted to the desired concentration. Characterization data of compound 2b is extensively discussed in the ESI (Fig. C.1 and C.2†).

### 2.5 Synthesis of 3-[3-(4-hydroxy-2-oxo-2*H*-chromen-3-yl)-allylidene]chromane-2,4-dione (3)

4-Hydroxy coumarin (2.0 eq.,  $2.0 \times 10^{-3}$  mol, 0.324 g) and malondialdehyde bis(diethyl acetal) (1.0 eq.,  $1.0 \times 10^{-3}$  mol, 0.220 g) were dissolved in dry acetonitrile ( $1.0 \times 10^{-3}$  L). Afterward, *p*-toluenesulfonic acid (2.0 eq,  $2.0 \times 10^{-3}$  mol, 0.280 g) as the catalyst was added. The reaction was completed after 5 minutes at 70 °C. The reaction mixture was filtered and the residue was washed with cold acetonitrile. A red powder was obtained in 95% yield (0.342 g). Characterization data of compound 3 is extensively discussed in the ESI (Fig. D.1 and D.2†).

### 2.6 Fluorescence titration of 3 with ions

A stock solution of compound 3 was prepared in ethanol to the final concentration of  $3.0 \times 10^{-3}$  M. This stock solution was diluted to the desired concentration. Chloride salts of the cations ( $\text{Sn}^{2+}$ ,  $\text{Fe}^{3+}$ ,  $\text{As}^{3+}$ ,  $\text{Li}^+$ ,  $\text{Ni}^{2+}$ ,  $\text{Ba}^{2+}$ ,  $\text{Hg}^{2+}$ ,  $\text{K}^+$ ,  $\text{Sn}^{2+}$ ,  $\text{Mn}^{2+}$ ,  $\text{Na}^+$ ,  $\text{Ca}^{2+}$ ,  $\text{Zn}^{2+}$ ,  $\text{Cd}^{2+}$ ,  $\text{Co}^{2+}$ ,  $\text{Al}^{3+}$ ,  $\text{Cu}^+$ ,  $\text{Cu}^{2+}$ ) and sodium salts of the anions ( $\text{Cl}^-$ ,  $\text{OAc}^-$ ,  $\text{NO}_3^-$ ,  $\text{SO}_4^{2-}$ ,  $\text{SCN}^-$ ,  $\text{PO}_4^{3-}$ , 10 eq.) were prepared in deionized water to afford  $2 \times 10^{-2}$  M aqueous solution. The ions were added to a solution of compound 3 in a quartz cell (path length of 1 cm). The change in the fluorescence spectrum of 3 at 480 nm was recorded immediately after preparing sample. All the experiments were conducted at room temperature. The excitation wavelength of 3 was 480 nm.

### 2.7 Cell culture and imaging

The breast cancer cell line MCF7, received from the Pasteur institute (Tehran, Iran), was grown in Dulbecco's Modified Eagle Medium (DMEM) supplemented with 10% (v/v) fetal bovine serum (FBS) and 1.5% (v/v) Penicillin-Streptomycin (Pen-Strep) at 37 °C in a humidified environment of 5%  $\text{CO}_2$ . Then cells were treated with  $2.5 \times 10^{-5}$  M of compound 3 in EtOH-water 2:3 (v/v) for 45 minutes at 37 °C, then incubated with  $\text{SnCl}_2$  (0.5, 0.1 and  $1.0 \times 10^{-4}$  M) for 60 minutes. The fluorescence images were obtained on a fluorescent microscope with an objective lens ( $\times 200$ ).

### 2.8 Cytotoxicity assays

In 96-well plate, 10 000 cells were seeded per well. One molar concentration of different components was prepared in 40% ethanol. Then, serial dilution of components was prepared in fresh medium. They were added triplicate after 24 h of seeding.



The incubation time was 24 h. The fresh medium containing 0.5 mg mL<sup>-1</sup> of MTT was added. Optical density was measured at 570 nm with solvent as blank using a Bio-Rad microplate reader. The negative control was the cell culture medium without components. The IC<sub>50</sub> (concentration for 50% cell growth inhibition) was calculated from the dose-response curve.

### 3 Result and discussion

#### 3.1 Design and synthesis of compounds 2–3

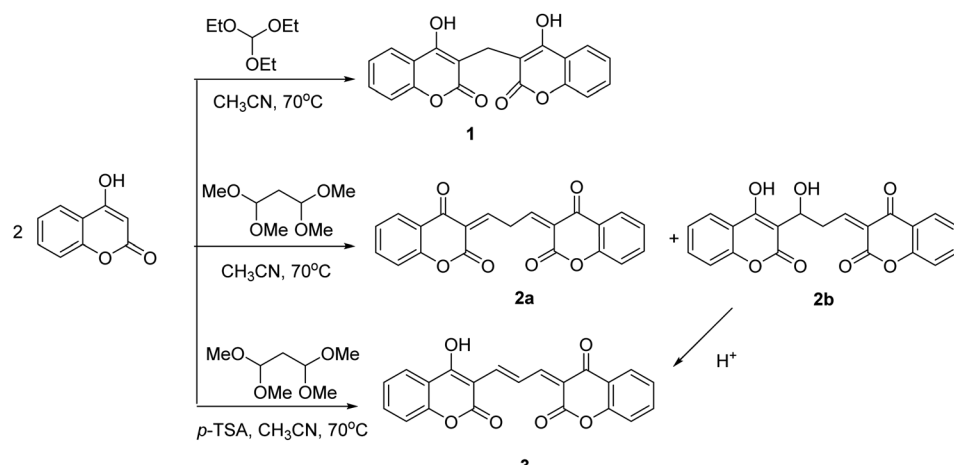
Coumarin is a natural product derived from plants and is known for its biological characteristics. The molecule is fluorescent over the emission range of 400–500 nm. Dicoumarol (**1**) is a natural anticoagulant bearing two equivalent coumarins, which are linked *via* a –CH<sub>2</sub>– group. As shown in Fig. E.1A,† the maximum emission wavelength of **1** is almost the same as the parent molecule, coumarin, since the connection between the two fluorescent motifs is through a methylene bridge. In the present study, we attached coumarins through conjugated  $\pi$  bonds. Extending the conjugation system shifted the emission wavelength to higher values. To this end, we used malondialdehyde bis(dimethyl acetal) to produce compound **2a** (Scheme 1). Exposure of **2a** to DMF or water converts it to **2b** in an irreversible manner. The higher emission intensity of **2b** compared with **2a**, makes the former more favorable for sensor design. Therefore, we evaluated several solvents and temperatures to find experimental conditions at which the transformation of **2a** to **2b** occurs at high rates. The results showed that the conversion of compound **2a** to compound **2b** in protic and aprotic solvents with different polarities occurs at different rates, and no order was observed. Also, using dried solvents and reducing the temperature significantly decreased the conversion speed. However, among the various conditions tested, incubating **2a** with DMF at RT for 4 h was the best for the completion of the reaction. The conversion of **2a** to **2b** was monitored in DMF with fluorescence spectroscopy. The evolution of the fluorescence emission upon dispersion of **2a** in DMF is represented in

Fig. E.1B,† As is shown, the emission of **2a** (0 min) is very weak, while **2b** has a strong emission intensity at the same concentration. The results showed that this conversion was completed by 4 hours at room temperature. NMR spectroscopy verified the conversion of **2a** to **2b** (Fig. F.1†). The <sup>1</sup>H NMR of **2a** was recorded in CDCl<sub>3</sub>, while that of **2b** was measured in DMSO-d<sub>6</sub>. The result confirmed that 92% of **2a** converted to **2b**.

In an acidic environment without any catalyst being involved, **2b** transformed to **3** (Scheme 1). So, we examined different acids such as HCl, *p*-TSA, CuCl, LiClO<sub>4</sub>. After confirming *p*-TSA as the best, the amount of the acid was determined, which showed the equivalent of *p*-TSA in the shortest time had the best results in the formation of product **3** from **2b**. Nevertheless, **3** can be directly prepared from the reactant and the linker in the presence of *p*-TSA. Both **2b** and **3** showed strong fluorescence emission in the visible range of the electromagnetic spectrum. In the following experiments, the binding affinity of the two compounds toward various metal ions was studied.

#### 3.2 Solvatochromic effect of **2b** and **3**

The solvatochromic effect was studied by the measurement of the emission profiles of **2b** and **3** in solvents with different polarities. The fluorescence spectra of compounds **2b** and **3** as well as the absorption spectra of **3** in solvents of different polarities at room temperature were recorded. In general, the solvent polarity decreases according to the order of water > methanol (MeOH) > ethanol (EtOH) > acetonitrile (CH<sub>3</sub>CN) > DMSO > DMF > acetone > ethyl acetate (EtOAc) > THF. Solvatochromism originates from the differences between the solvation energy of the initial and excited state of the dye in various solvents. Accordingly, we observed that the absorption and emission profiles of both dyes strongly depend on the solvent. UV-Vis absorption and fluorescence spectroscopy confirmed the solvatochromic effect of **3** (Fig. G.1†). We used solvents of distinct polarity. Fig. G.1A† shows solvent-dependent peak shift. Except for DMSO and DMF, which shows a reverse trend, with decreasing solvent polarity (EtOH :



Scheme 1 Synthesis route of compounds 1–3.



$\text{H}_2\text{O}$  (2 : 3) > EtOH :  $\text{H}_2\text{O}$  (2 : 1) > MeOH > EtOH > DMSO > DMF), the maximum emission wavelength shows a red shift from 569 nm to 580 nm. Fig. G.1A† also illustrates that compound 3 does not emit light in certain solvents (THF, EtOAc,  $\text{CH}_2\text{Cl}_2$ , acetone,  $\text{CH}_3\text{CN}$ , EtOH :  $\text{H}_2\text{O}$  (1 : 5)). The measured stock shift of compound 3 in EtOH/water (2 : 3 v/v) was 42 nm ( $\lambda_{\text{ex}} = 480$  nm,  $\lambda_{\text{em}} = 570$  nm,  $\lambda_{\text{abs}} = 528$ ). The peak shift is also observed in the UV-Vis absorption profile of 3 (Fig. G.1B†). The spectral shift of 3 in Fig. G.1B† almost follows the order of solvent polarity. Except for DMF, which does not show a reasonable trend, with decreasing polarity from methanol to THF, the absorption peak shows a redshift of 8 nm.

In the case of 2b, it is notable that this compound mostly solubilizes in DMF. Therefore, to study the solvatochromic effect, we prepared a solvent mixture in such a way that DMF was used as a co-solvent with a volume ratio of 1 : 5 (DMF : solvent (x)). The results showed with increasing the solvent polarity, the fluorescence intensity of 2b decreased, and the maximum emission wavelength showed a slight shift to lower values (Fig. G.2†). An exception of the wavelength shift was observed for water, at which case the shift was toward the opposite direction. It is possible that other type of solvent-solute interactions is present in water.<sup>36</sup> The stock shift in the DMF/water (1 : 5 v/v) was 32 nm ( $\lambda_{\text{ex}} = 470$  nm,  $\lambda_{\text{em}} = 565$  nm, and  $\lambda_{\text{abs}} = 533$  nm). Similar to 3, the UV-Vis spectral shift of 2b

with decreasing solvent polarity directed toward longer wavelengths (data not shown). According to the UV-Vis absorption spectroscopy, the solvatochromic behavior of 2b and 3 was similar.

### 3.3 Ion sensing property of 2b and 3

2b was added to a standard solution of each ion ( $\text{Fe}^{3+}$ ,  $\text{As}^{3+}$ ,  $\text{Li}^+$ ,  $\text{Ni}^{2+}$ ,  $\text{Ba}^{2+}$ ,  $\text{Hg}^{2+}$ ,  $\text{K}^+$ ,  $\text{Sn}^{2+}$ ,  $\text{Mn}^{2+}$ ,  $\text{Na}^+$ ,  $\text{Ca}^{2+}$ ,  $\text{Zn}^{2+}$ ,  $\text{Cd}^{2+}$ ,  $\text{Co}^{2+}$ ,  $\text{Al}^{3+}$ ,  $\text{Cu}^+$ ,  $\text{Cu}^{2+}$ ,  $\text{Cl}^-$ ,  $\text{OAc}^-$ ,  $\text{NO}_3^-$ ,  $\text{SO}_4^{2-}$ ,  $\text{SCN}^-$ ,  $\text{PO}_4^{3-}$ , 10 eq.) to determine their contribution in signal change (Fig. 1A). The result showed that the signal of 2b did not change, except, partially, for  $\text{Fe}^{2+}$ . The selectivity of 3 toward the same ions were tested. We observed that,  $\text{Sn}^{2+}$  quenched the fluorescence signal of 3 almost completely.  $\text{Fe}^{2+}$  and, to some extent,  $\text{Fe}^{3+}$  quenched the fluorescence signal possibly due to their strong quenching behavior and paramagnetic properties.<sup>12,37,38</sup> A competitive study was carried out with the co-existence of other metal ions. To this end, the fluorescence spectra of compound 3 +  $\text{Sn}^{2+}$  (10 eq.) in the presence of other cations and anions (10 eq.) as coexisting species were measured. As shown in Fig. 1B, the response of 3 to  $\text{Sn}^{2+}$  was almost identical to the signal observed in the presence of  $\text{Sn}^{2+}$  + other ions. Overall, the data in Fig. 1 demonstrates high selectivity of 3 toward  $\text{Sn}^{2+}$ .

Table 1 compares the analytical performance of 3 to other probes used for the optical determination of metal ions. The

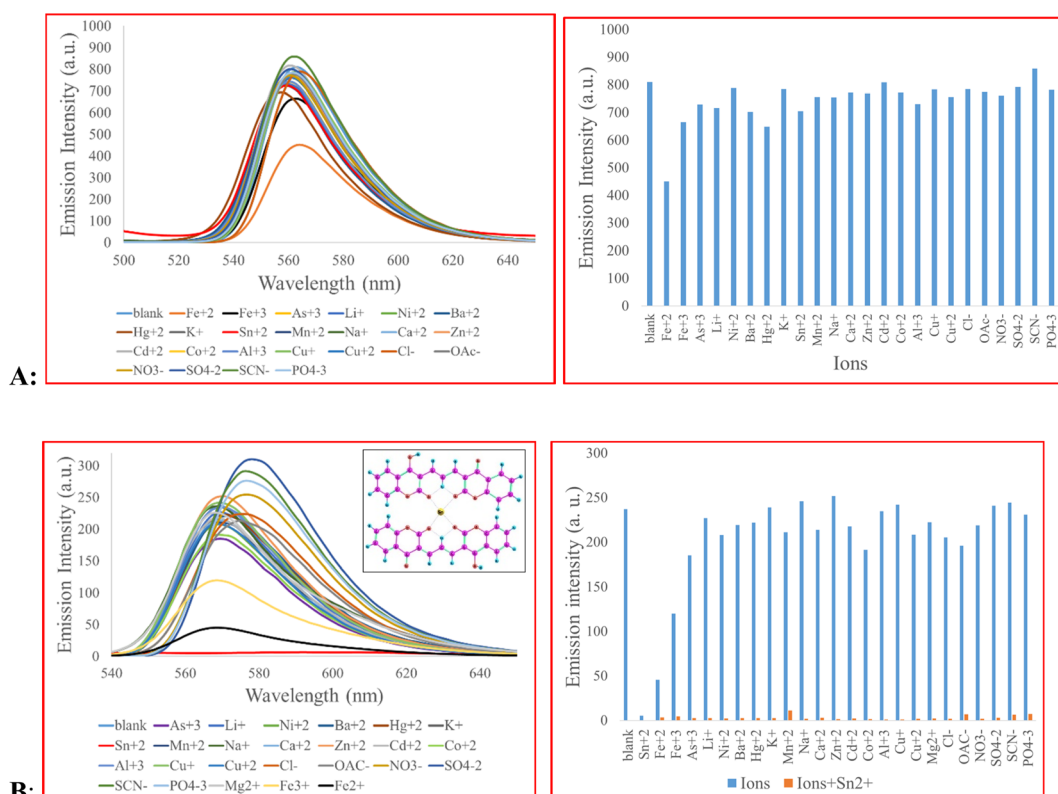


Fig. 1 (A) Fluorescence emission of 2b ( $5.0 \times 10^{-5}$  M) in the presence of different ions (10 eq.). 2b was solubilized in DMF– $\text{H}_2\text{O}$  (1/5, v/v) with  $\lambda_{\text{ex}}$  of 470 nm; (B) fluorescence emission of 3 ( $5.0 \times 10^{-5}$  M) in response to various ions (10 eq.). 3 was solubilized in EtOH– $\text{H}_2\text{O}$  (2/3, v/v) with  $\lambda_{\text{ex}}$  of 480 nm. The concentration of sodium and potassium ions is 34 mM and 120 mM, respectively, equal to the values found in normal lymphocytes.<sup>39</sup>



Table 1 Comparison between the analytical performance of 3 and other fluorophores

Fluorophore	Metal ion	Detection mode	Detection limit	Interferences	References
4-Phenyl-2-(2'-pyridyl) quinoline	Fe <sup>3+</sup>	Turn on (Fe <sup>3+</sup> )	Fe <sup>2+</sup> : $8.772 \times 10^{-9}$ mol L <sup>-1</sup>	Fe <sup>2+</sup> interferes the detection of Fe <sup>3+</sup> and vice versa	44
	Fe <sup>2+</sup>	Turn off (Fe <sup>2+</sup> )	Fe <sup>3+</sup> : $1.912 \times 10^{-9}$ mol L <sup>-1</sup>		
A naphthol hydrazone Schiff base bearing benzothiadiazole	Fe <sup>3+</sup>	Turn off	0.036 μM	—	45
A composite film containing (18-crown-6)-styrylpyridine	Hg <sup>2+</sup>	Fluorescence signal blue shift	$10^{-8}$ mol L <sup>-1</sup>	—	46
Anthracene benzene conjugate	Ag <sup>+</sup>	Turn off	1.4 nM	Bi <sup>3+</sup>	47
2,2'-Bipyridyl acylhydrazone Schiff base	Cu <sup>2+</sup>	Turn off	$2.7 \times 10^{-6}$ mol L <sup>-1</sup>	Zn <sup>2+</sup> enhances the signal	40
[(Z)-2-((Pyren-1-ylmethylene)amino)phenol]	Ga <sup>3+</sup>	Turn on	3.35 nM	The interference of Fe <sup>2+</sup> or Fe <sup>3+</sup> is not investigated	48
1-(6-Aminopyridin2-yl)-3-phenylthiourea	Hg <sup>2+</sup> , Ag <sup>+</sup> , Au <sup>3+</sup>	Turn on	5.01 × 10 <sup>-7</sup> M for Hg <sup>2+</sup> 2.14 × 10 <sup>-8</sup> M for Ag <sup>+</sup> 34 × 10 <sup>-7</sup> M for Au <sup>3+</sup>	Each target ion interferes with the fluorescence signals of the others	49
2-Hydroxy-naphthalene hydrazone based probe	Cu <sup>2+</sup> and Al <sup>3+</sup>	Colorimetric for Cu <sup>2+</sup> Fluorometric for Al <sup>3+</sup>	0.4 μM for Cu <sup>2+</sup> 14 nM for Al <sup>3+</sup>	Al <sup>3+</sup> interferes with the colorimetric signal of Cu <sup>2+</sup>	50
Macroacyclic Schiff base ligand ((1E)-1-(2-methylphenyl)-N-[2-(4-{2-[{E}-[(2-methylphenyl)methylidene]amino]phenyl}-1,4-diazepan-1-yl)phenyl]methani mine)	Al <sup>3+</sup>	Turn on	$2.1 \times 10^{-9}$ M	Cu <sup>2+</sup> , Sn <sup>2+</sup> , Fe <sup>2+</sup> , Fe <sup>3+</sup>	51
1,2-Alternate thiocalix [4]arene-based fluorophore	Ag <sup>+</sup>	Turn off	$7.6 \times 10^{-9}$ M	The interference of Fe <sup>2+</sup> is not investigated, Al <sup>3+</sup> interferes	52
Anthracene-based Schiff base 2-(anthracen-9-ylmethylene)-N-methylhydrazine-1-carbothioamide	Ag <sup>+</sup>	Turn off	$5.95 \times 10^{-7}$ M	—	53
Naphthalene based fluorophores (OHHN)	Al <sup>3+</sup>	Turn on	$0.176 \times 10^{-5}$ M	—	54
4-Vinyl substituted triphenylamine	Hg <sup>2+</sup>	Turn off	0.146 μM	Fe <sup>2+</sup>	55
Styrylflavilium dye with a di-(2-picolyl) amine (DPA) moiety as the metal chelating unit	Zn <sup>2+</sup>	Turn off	0.39 μM	Cu <sup>2+</sup>	56
(E)-4-Methyl-N-((2,3,6,7-tetrahydro-1H,5H-pyrido[3,2,1-ij]quinolin-9-yl)methylene)benzenesulfonohydrazide	Bi <sup>3+</sup>	Fluorescence (Turn on) UV-Vis (from colorless to crimson yellow)	6.39 nM 170 nM	The interference of Fe <sup>2+</sup> is not investigated	57
1,4-Bis((ferrocenylidenehydrazone)methyl)benzene	Cu <sup>2+</sup>	Turn on	$4.2 \times 10^{-6}$ M	—	41
N-(Pyrimidin-2-yl) thiophene-2-carboxamide	Fe <sup>3+</sup>	Fluorescence (turn off) UV-Vis (color change from colorless to yellow)	1.24 μM 2.03 μM	—	42
2-(2'-Hydroxyphenyl) benzothiazole derivative Coumarin-Schiff base compounds	Cd <sup>2+</sup> Co <sup>2+</sup> Ni <sup>2+</sup> Cu <sup>2+</sup>	Turn on Turn off	1.16 μM 0.11 μM 0.09 μM 0.24 μM	Zn <sup>2+</sup> Co <sup>2+</sup> Ni <sup>2+</sup> Cu <sup>2+</sup>	43 58
Coumarin-Picolinohydrazone derived Schiff base Coumarin azo dye	Al <sup>3+</sup> Cu <sup>2+</sup>	Turn on Colorimetry	0.0490 μM 0.0779 mg L <sup>-1</sup>	Cu <sup>2+</sup> , Fe <sup>2+</sup>	59 60
Polyurethane nanoemulsion bearing coumarin derivative (PU-co-HCCA)	Hg <sup>2+</sup>	Turn on	1.61 ppb	—	61
TPPB	Sn <sup>2+</sup> Sn <sup>2+</sup>	Turn on Turn on	0.116 μM 79 nM	—	20 62



Table 1 (Contd.)

Fluorophore	Metal ion	Detection mode	Detection limit	Interferences	References
2-(4-Chlorophenyl)-N-(4-((4-dioxo-3-(thiophen-2-ylthio)-1,4-dihydronaphthalen-2-yl)amino) phenyl)sulfonylphenylacetamide	$\text{Sn}^{2+}$	Turn on	0.115 $\mu\text{M}$	—	63
4-((3-Chloro-1,4-dioxo-1,4-dihydronaphthalen-2-yl)amino)benzenesulfonamide	$\text{Sn}^{2+}$	Turn on	$2.6 \times 10^{-8}$ mol $\text{L}^{-1}$	—	64
Rhodamine-triazole-pyridine ternary conjugation	$\text{Sn}^{2+}$	Turn on	$5.4 \times 10^{-6}$ M	—	65
1-Aminopyrene and 5-bromo-2-thiophene carboxaldehyde Coumarin derivative	$\text{Sn}^{2+}$	Turn off	$3.89 \times 10^{-6}$ M	$\text{Fe}^{2+}$ , $\text{Fe}^{3+}$	This work

one-step synthesis of **3** is accomplished under mild experimental condition and a short time. The starting material and the product are not toxic. Our probe is highly selective toward  $\text{Sn}^{2+}$ . Except for  $\text{Fe}^{2+}$  and partially  $\text{Fe}^{3+}$ , no ion is interfering in signal quenching. The selectivity of **3** is better or comparable to most of the reported probes in Table 1. While some reports determined metal ions down to nanomolar concentration, our LOD value is in the micromolar concentration range, similar to ref. 40–43. Besides, the fluorescence signal of our probe is stable under physiological conditions and it can penetrate into the living cells.

To gain more information about the sensing behavior of compound **3** toward  $\text{Sn}^{2+}$ , the fluorescence titration experiment was performed. For this purpose, emission spectra of **3** upon the addition of  $\text{Sn}^{2+}$  ion were recorded (Fig. 2). As a result, with the increasing concentration of  $\text{Sn}^{2+}$ , the fluorescence intensity gradually decreased. The measured detection limit (LOD =  $3\sigma/m$ ) was  $3.89 \times 10^{-6}$  M. The probe responded immediately after the addition of  $\text{Sn}^{2+}$  and its signal reached a plateau after 10 min (Fig. H.1†). We evaluated the reversibility of the system by adding EDTA, as a strong chelating reagent, to a solution of **3** +  $\text{Sn}^{2+}$ . Fig. H.1 in the ESI† shows that the signal restores by 79% of its initial value showing system reversibility.

The quenching behavior of **3** in response to  $\text{Sn}^{2+}$  was studied by Stern–Volmer equation (eqn (1))

$$F_0/F = 1 + K_{\text{SV}} [\text{Q}] \quad (1)$$

$F_0$  and  $F$  are the fluorescence intensity before and after the addition of the quencher, respectively, and  $[\text{Q}]$  is the quencher concentration.  $K_{\text{SV}}$  is the Stern–Volmer quenching constant, which in case of dynamic (collisional) quenching is expressed as  $K_{\text{D}}$ . On the other hand, when the quenching is static,  $K_{\text{SV}}$  is designated as an association constant ( $K_{\text{S}}$ ). A linear Stern–Volmer plot indicates that either dynamic or static quenching occurs between the quencher and fluorophore (Fig. 3A).<sup>66</sup> However, to determine which mechanism is involved in the quenching process, we compared the absorption profile of **3** before and after the addition of  $\text{Sn}^{2+}$  (Fig. 3B and C).<sup>66</sup> After adding  $\text{Sn}^{2+}$ , the intensity of the maximum absorption peak of **3** decreased. To obtain the difference spectrum, however, we normalized both spectra (Fig. 3B) and calculated the difference spectrum by point-by-point subtraction. As shown in Fig. 3C, a decrease in absorbance at 460 nm and an absorbance increase at 541 nm is observed, indicating the change in the absorbance spectrum of the fluorophore. Besides, the high value of  $K_{\text{SV}}$  indicates static quenching.<sup>66,67</sup> In the present study, the magnitude of  $K_{\text{SV}}$  is  $4.1 \times 10^3$ . Therefore, we speculate that the mechanism of quenching is static quenching.

Job's plot analyses determined the binding stoichiometry of compound **3** with  $\text{Sn}^{2+}$  via analyzing the different  $\text{Sn}^{2+}$

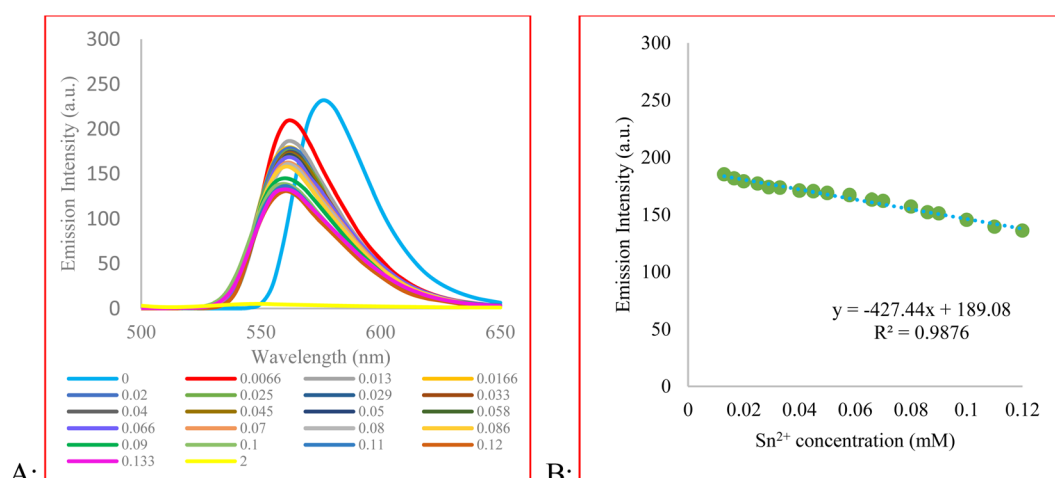


Fig. 2 (A) Fluorescence spectra of compound **3** ( $2.0 \times 10^{-4}$  M) with the addition of various concentrations of  $\text{Sn}^{2+}$  (0–0.2 mM,  $\lambda_{\text{ex}} = 480$  nm). (B) The  $\text{SnCl}_2$  concentration effect on fluorescence quenching.



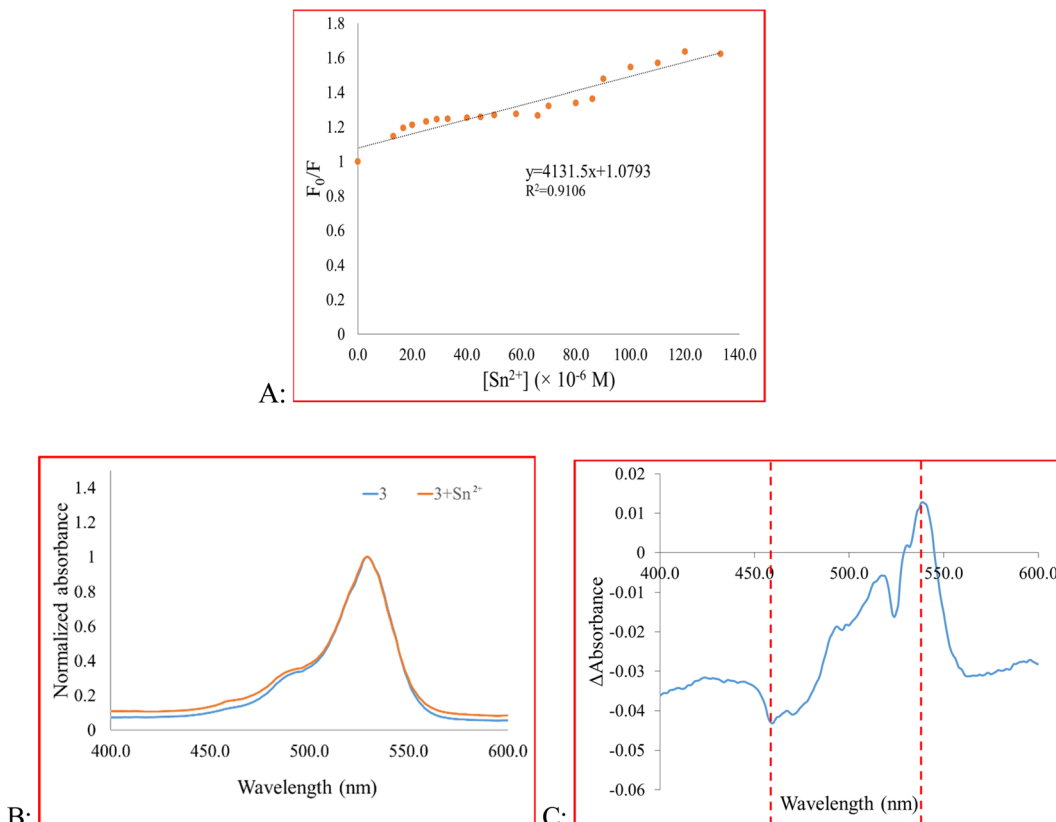


Fig. 3 (A) Fluorescence quenching behavior of **3**, (B) the absorbance spectra of **3** and **3** +  $Sn^{2+}$ , (C) the difference spectrum of **3** and **3** +  $Sn^{2+}$ .

concentrations' effect on fluorescence emission intensity changes. The maximum fluorescence change is produced when the molar fraction of  $Sn^{2+}$  is close to 0.4, indicating that the binding ratio of compound **3** to  $Sn^{2+}$  is 2 : 1 (Fig. 4).

The FT-IR analysis of **3** +  $Sn^{2+}$  strongly endorses complex formation (Fig. I.1†). The stretching vibration frequency of the esteric C=O ( $1718\text{ cm}^{-1}$ ) shifted to the lower frequency region ( $1711\text{ cm}^{-1}$ ) due to the reduction of the electron density,

whereas stretching vibration frequencies of OH ( $3467\text{ cm}^{-1}$ ) and ketonic C=O ( $1636\text{ cm}^{-1}$ ) are relatively unchanged. This data indicated that complexation has occurred from the esteric functional group of the coumarin framework. The typical absorptions for Sn–O vibration in the complex are located in the normal range  $420\text{--}480\text{ cm}^{-1}$ , which can be seen as a broad signal and more intense than the compound **3** signal in this region. The binding behavior of  $Sn^{2+}$  could be rationally explained by acid–base principle.  $Sn^{2+}$  is a soft acid with electrophilic properties. It preferentially coordinates with the electronegative soft base of oxygen.

### 3.4 Biological assessment

**3.4.1 Cytotoxicity.** The cytotoxic effect of compounds **1**–**3** is shown in Fig. 5. The  $IC_{50}$  of **1**, **2**, **3**, and 4-hydroxy cumarin (reactant) are  $760$ ,  $24$ ,  $711$ , and  $511\text{ }\mu\text{M}$ , respectively. These  $IC_{50}$  values show that **3** (the coumarin-derived product) is safe for use in biological systems.

**3.4.2 Fluorescence microscopy.** The MCF7 cells were pre-treated with the probe ( $2.5 \times 10^{-5}\text{ M}$ ) in EtOH : Water 2 : 3 (v/v) at  $37\text{ }^\circ\text{C}$  for 60 min to test the ability of compound **3** for live-cell imaging. The extra amount of the probe was removed by three times washing with PBS (pH = 7.2). Cells were also stained by DAPI as a nucleus-specific dye in the blue filter (Fig. 6). The MCF7 cells were further incubated with  $SnCl_2$  ( $100\text{ }\mu\text{M}$ ). 5 to 30 min later, the fluorescence images were obtained on a fluorescent microscope with an objective lens ( $\times 200$ ). Probe is

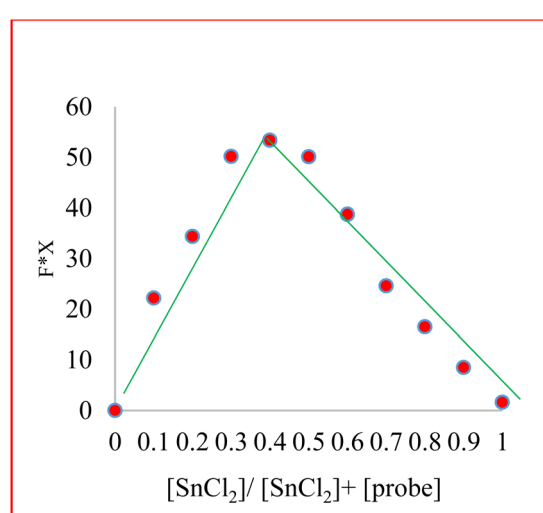


Fig. 4 Job's plot for the complex formation between **3** with  $Sn^{2+}$ .

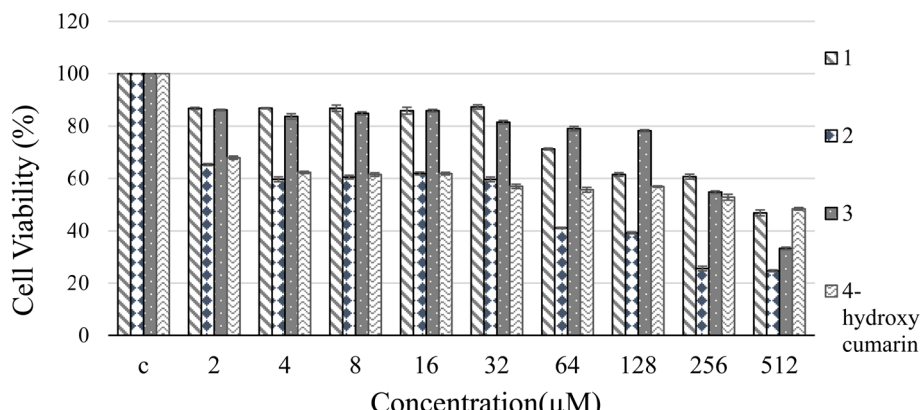


Fig. 5 Cytotoxicity of compound 1–3 against MCF-7 cells.

located in nucleus and cytoplasm with higher aggregation in nucleus (Fig. J.1†). A significant decrease in the probe's fluorescence signal was observed after incubating cells with  $\text{SnCl}_2$  (Fig. 7). These results indicate that the probe is cell membrane

permeable and can respond to the added  $\text{SnCl}_2$  in the living cells. Studies showed that tin compounds have genotoxicity, resulting in DNA damage and chromosomal aberrations.<sup>7</sup> So, this probe can be used to detect tin pollution in cells. Notably,

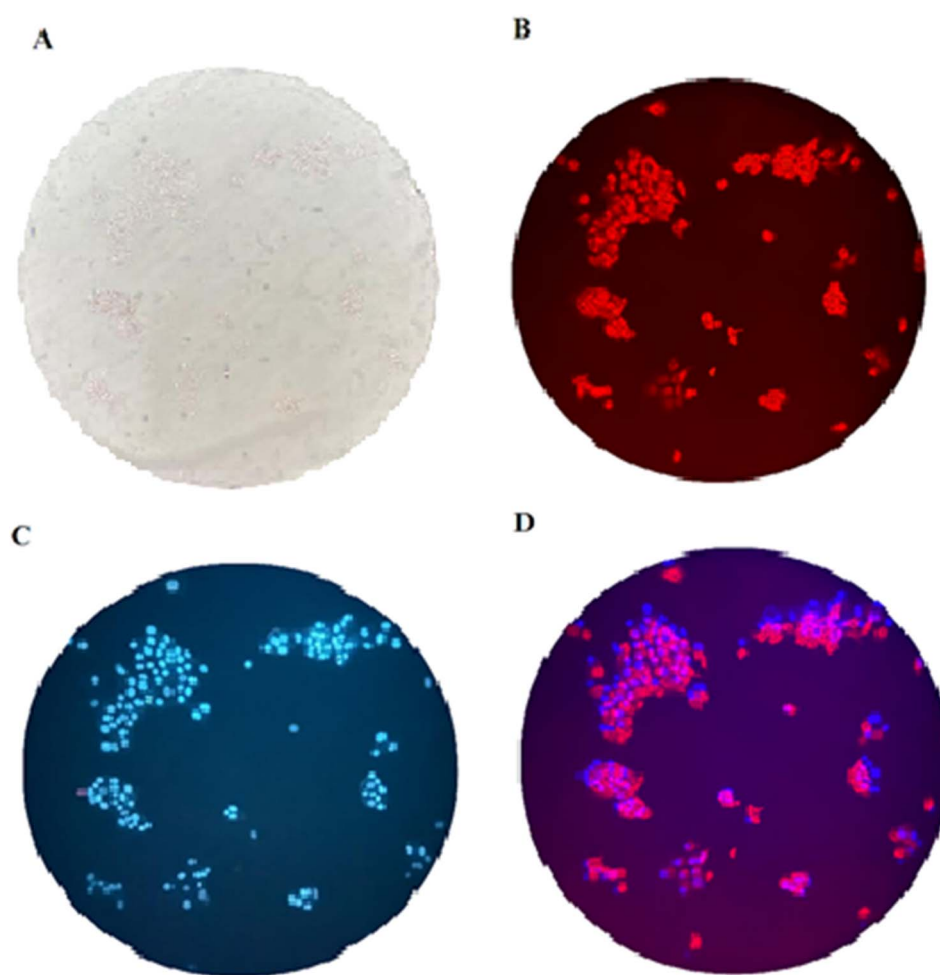


Fig. 6 Bright-field microscopy images of the probe in MCF7 cells (A). The cells were incubated with a probe ( $2.5 \times 10^{-5}$  M) for 60 min at 37 °C and washed with PBS three times (B). DAPI staining (C). Red emission was collected at  $645 \pm 75$  nm; Blue emission was collected at  $470 \pm 40$  nm. Digitally merged image (D).



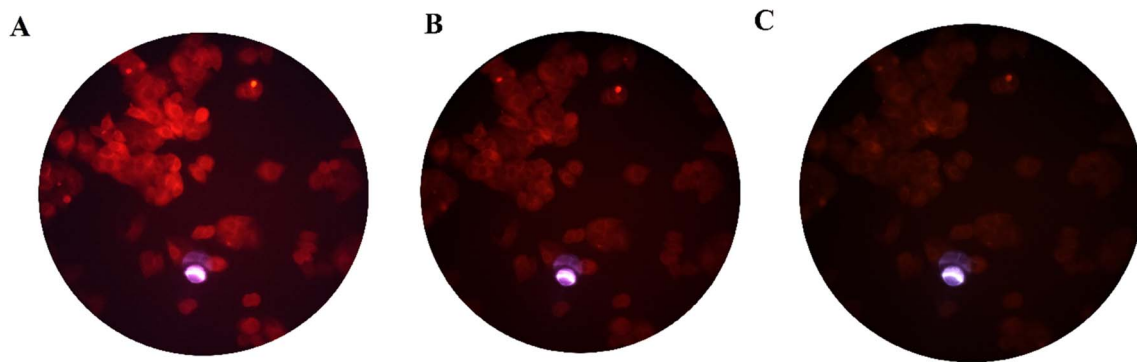


Fig. 7 The MCF7 cells with  $(2.5 \times 10^{-5}$  M) probe were further incubated with  $\text{SnCl}_2 1.0 \times 10^{-4}$  M (A). 10 to 30 min later, the fluorescence images were obtained on a fluorescent microscope with an objective lens ( $\times 200$ ). A significant decrease in the probe's fluorescence signal was observed after incubating cells with  $\text{SnCl}_2$  (B and C).

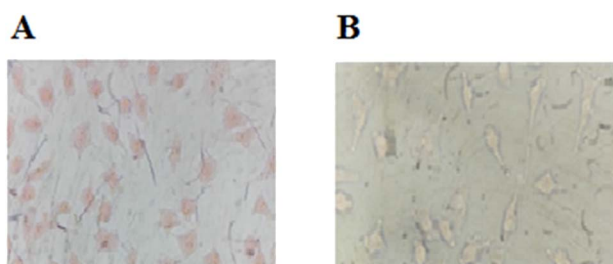


Fig. 8 Bright field microscopic images of the probe in MCF7 cells. The cells were incubated with probe  $(2.5 \times 10^{-4}$  M) (A) for 60 minutes at  $37^\circ\text{C}$  and washed with PBS 3 times. Then the cells were treated and incubated with  $\text{SnCl}_2$  ions  $1.0 \times 10^{-4}$  M for 15 minutes at  $37^\circ\text{C}$  (B).

the cells became red under visible light in the first minute after staining. This property can be used for the colorimetric study of  $\text{SnCl}_2$  sensing. For this purpose, the image was obtained on a light microscope with an objective lens ( $\times 200$ ) (Fig. 8).

### 3.5 Theoretical calculations

To rationalize the sensing behavior of compound 3 toward  $\text{Sn}^{2+}$  and the quenching of its fluorescence signal in the presence of

$\text{Sn}^{2+}$ , we have performed a computational study in the framework of density functional theory (DFT). In a computational study, the choice of a proper calculation level is an important task that should be carried out with care to ensure the reliable prediction of electronic and optical properties. To this end, we have examined six functions belonging to different categories of DFT to choose the best method for our study. The examined functions were assessed for reproducing the experimental fluorescence emission signal of compound 3 ( $\lambda_{\text{max}} = 560$  nm). The geometry of the molecules was optimized at the first singlet excited state using the time-dependent DFT (TD-DFT) approach as implemented in Gaussian 09 package to simulate the fluorescence spectra.<sup>68</sup> The implicit solvent effect has been included by employing the polarizable continuum model (PCM)<sup>69</sup> within  $\text{EtOH}-\text{H}_2\text{O}$  (2/3) medium. The results (Fig. K.1 in the ESI†) indicated that the hybrid B3LYP functional remarkably outperforms other tested functionals, and its result for the maximum emission wavelength of compound 3 ( $\lambda_{\text{max}} = 534$  nm) is in better agreement with the measured experimental value. Accordingly, all calculations were performed using the B3LYP functional and triple zeta valence plus polarization (TZVP) basis set.

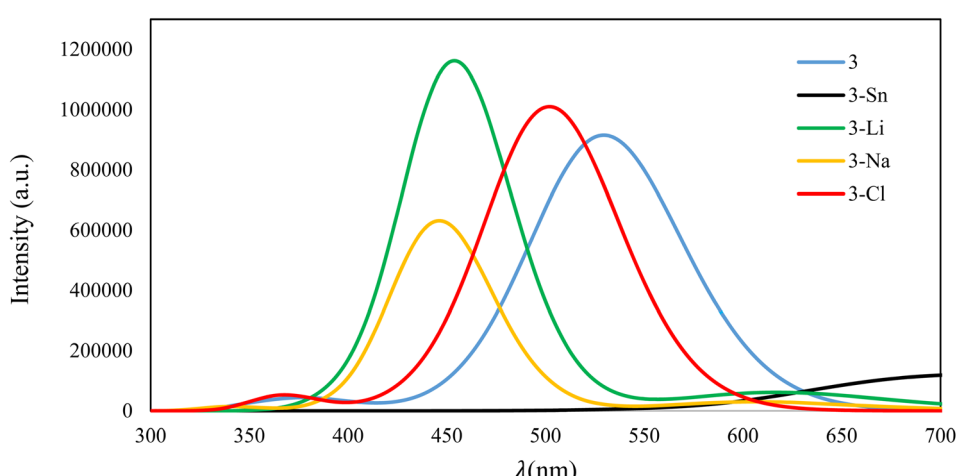


Fig. 9 Fluorescence emission of 3 and its complexes with  $\text{Sn}^{2+}$ ,  $\text{Li}^+$ ,  $\text{Na}^+$ , and  $\text{Cl}^-$  ions in  $\text{EtOH}-\text{H}_2\text{O}$  (2/3) solvent.



To gain deep insight into the sensing behavior of compound 3 toward  $\text{Sn}^{2+}$ , we have compared the fluorescence emission of 3 in response to  $\text{Sn}^{2+}$  with its responses to three representative ions such as  $\text{Li}^+$ ,  $\text{Na}^+$ , and  $\text{Cl}^-$ . For reliable estimation of fluorescence emission wavelength, finding the correct geometry and the global minima of the complexes between compound 3 and ions on the potential energy surface is the first requirement. Accordingly, several possible initial configurations were constructed by aligning the considered ions on different adsorption sites of compound 3. Then, full geometrical optimizations without any symmetry constraint were performed and after relaxation, the most stable complexes were identified by comparing the adsorption energies. The optimized structures for the 3-ions complexes in their lowest energy configurations and the calculated adsorption energies are shown in Fig. L1.†

The adsorption energies were calculated as the difference between the total energy of 3-ions complexes and the sum of energies of isolated 3 and ion fragments. The calculated adsorption energies follow the order of  $3\text{-Sn}^{2+} \gg 3\text{-Na}^+ > 3\text{-Li}^+ > 3\text{-Cl}^-$ . The trend shows that the 3- $\text{Sn}^{2+}$  complex is highly stable and its adsorption energy can be in the order of a chemical bond. The optimized configuration of 3- $\text{Sn}^{2+}$  confirms the strong binding between compound 3 and  $\text{Sn}^{2+}$  by forming two

Sn–O bonds. For further evidence, we simulated the IR spectra of 3- $\text{Sn}^{2+}$  complex and the Sn–O vibration band located in  $477\text{ cm}^{-1}$  was observed. In the case of  $\text{Li}^+$  and  $\text{Na}^+$ , the cation is also positioned in the same plane of coumarins but taking a larger distance from the oxygen of  $\text{C}=\text{O}$  group resulting in weaker interaction. The adsorption energies for 3- $\text{Li}^+$  and 3- $\text{Na}^+$  complexes are about 8 to 10 times less than that of 3- $\text{Sn}^{2+}$  complex. By contrast,  $\text{Cl}^-$  is located above the molecular plane with an adsorption energy of less than 1 kcal  $\text{mol}^{-1}$ , which is in the order of weak der Waals interactions. Based on the obtained results, it seems that the difference in the adsorption configuration and the binding strength might be responsible for the difference between the sensing behaviors of compound 3 toward various cations and anions.

Fig. 9 presents the fluorescence emission spectra of isolated compound 3 and its complexes with four examined ions recorded in  $\text{EtOH-H}_2\text{O}$  (2/3) media. As evident, after the adsorption of ions, the intensity of the fluorescence peak of the resultant complex depends on the interaction strength between 3 and ions. The strong binding between 3 and  $\text{Sn}^{2+}$  leads to complete quenching of the fluorescence signal, while complexes having weak interactions (3- $\text{Li}^+$ , 3- $\text{Na}^+$ , and 3- $\text{Cl}^-$ ) still show fluorescence signals in the visible region.

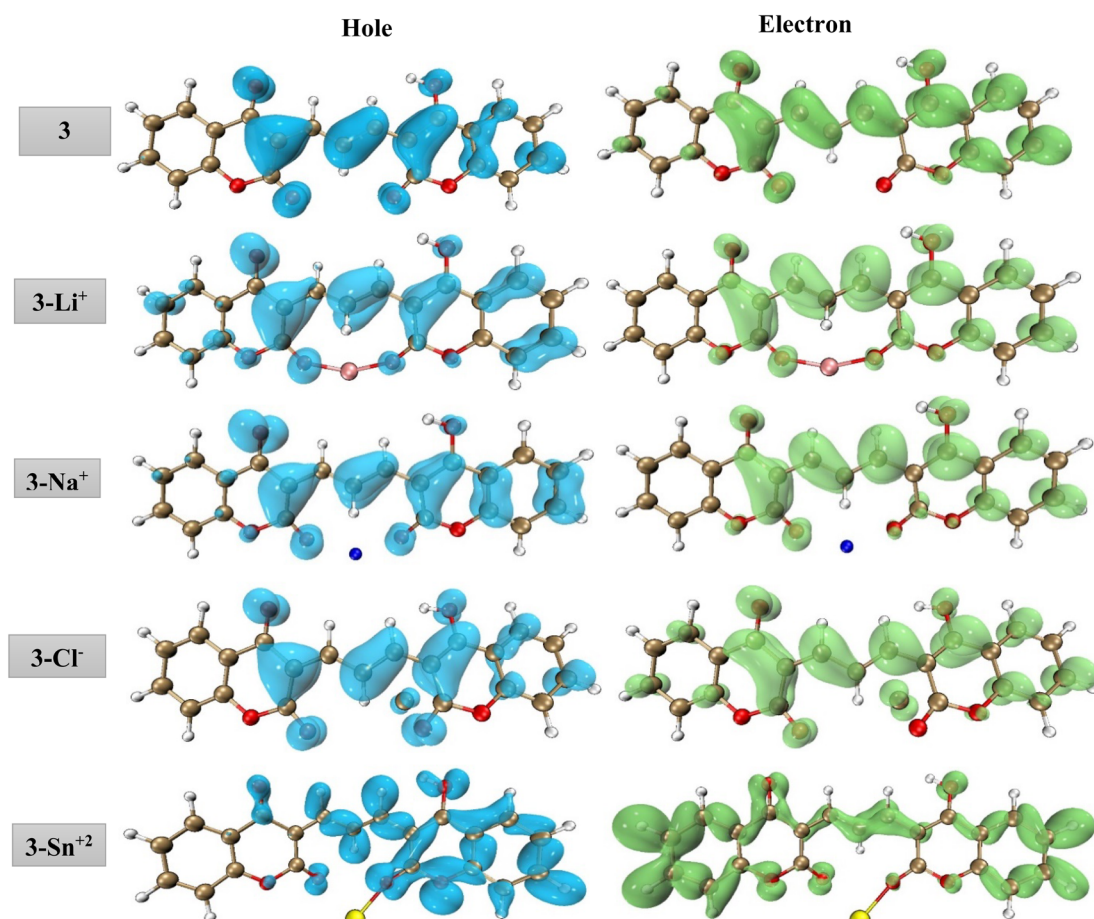


Fig. 10 Real-space representation of hole (blue) and electron (green) distributions for the main transitions of 3 and its complexes with  $\text{Sn}^{2+}$ ,  $\text{Li}^+$ ,  $\text{Na}^+$ , and  $\text{Cl}^-$  (isovalue = 0.001).



To provide more insight into the origin of the fluorescence peak, we performed hole–electron analysis which gives a definitive picture of the hole and electron distribution for any emission peak, by describing where the excited electron leaves (hole) and arrives (electron). The cube grid information on the hole–electron distribution was generated using the Multiwfns package,<sup>70</sup> followed by their visualization using the VMD software.<sup>71</sup> The hole and electron distributions associated with the fluorescence peak of the isolated compound **3** and its complexes with  $\text{Sn}^{2+}$ ,  $\text{Li}^+$ ,  $\text{Na}^+$ , and  $\text{Cl}^-$  ions are presented in Fig. 10. The fluorescence emission of compound **3** exhibits one main typical fluorescence band centered at 534 nm which is associated with the  $\pi \rightarrow \pi^*$  transition within the pyranone moiety and the  $\pi$  conjugation extension between two coumarins. Fig. 10 shows that in **3**– $\text{Li}^+$ , **3**– $\text{Na}^+$ , and **3**– $\text{Cl}^-$  complexes, the hole–electron distribution resembles compound **3** indicating that the adsorption of  $\text{Li}^+$ ,  $\text{Na}^+$ , and  $\text{Cl}^-$  does not change the electronic properties of free-standing compound **3**. It means no significant charge transfer occurs during the complex formation. By contrast, for the **3**– $\text{Sn}^{2+}$  complex, the hole and electron pattern is completely different from those of isolated **3** with the higher contribution of  $\sigma \rightarrow \sigma^*$  transition. It seems that the bond formation between Sn and oxygen leads to electron transfer from the  $\pi$  orbitals and redistributes the electronic density within the dicoumarol. As the  $\sigma \rightarrow \sigma^*$  transition requires higher energy thus does not fall in the visible range and just quenching of  $\pi \rightarrow \pi^*$  transition is observable.

## 4 Conclusion

In summary, biocompatible coumarin-based fluorophores were synthesized, and their photophysical properties were investigated. Among 18 different cations (including  $\text{Sn}^{2+}$ ) and 6 anions, compound **3** exhibited an immediate and selective fluorescence quenching behavior toward  $\text{Sn}^{2+}$ . The binding stoichiometry of **3** to  $\text{Sn}^{2+}$  was 2 : 1, according to the Job's plot. FTIR study revealed that the complexation proceeds through binding the ligand's esteric carbonyl to  $\text{Sn}^{2+}$  ions. Based on the value of  $K_{\text{SV}}$  and UV-Vis absorption studies, a static quenching was verified. According to the MTT results, the  $\text{IC}_{50}$  value of **3** was calculated as 711  $\mu\text{M}$ , which made it suitable for cellular imaging. Due to the widespread use of tin(n) chloride in industry, and its importance in DNA damage studies, we propose that **3** is an appropriate fluorescent probe for the colorimetric and fluorimetric detection of tin ions in the environment and in cellular media.

## Author contributions

Hamide Hosseini-Jani-Pirdehi: chemistry experiment, writing – original draft. Soodeh Amigh: theoretical calculation. Afshan Mohajeri: theoretical calculation. Elahe Nazeri: biological experiment. Amir Taheri: chemistry experiment, conceptualization. Keivan Majidzadeh-A: conceptualization. Zahra Mohammadpour: methodology, data curation, reviewing and editing. Rezvan Esmaeili: biological conceptualization, grant receiving and biological editing.

## Conflicts of interest

All authors declare no conflict of interest.

## Acknowledgements

This work was supported by the National Institute for Medical Research Development, NIMAD, with the foundation number 957590 and Motamed Cancer Institute (MCI).

## References

- 1 M. E. Conti, in *Mineral Components in Foods*, CRC press, 2006, pp. 339–362.
- 2 M. Hoch, *Appl. Geochem.*, 2001, **16**, 719–743.
- 3 I. Rajan, N. Narayanan, R. Rabindran, P. R. Jayasree and P. R. Manish Kumar, *Biol. Trace Elem. Res.*, 2013, **155**, 455–459.
- 4 J. C. P. De Mattos, V. C. d. Matos, M. P. Rodrigues, M. B. N. d. Oliveira, F. J. S. Dantas, S. D. Santos-Filho, M. Bernardo-Filho and A. Caldeira-de-Araujo, *Molecules*, 2012, **17**, 12974–12983.
- 5 E. S. Motta, P. T. Souza-Santos, T. R. Cassiano, F. J. S. Dantas, A. Caldeira-de-Araujo and J. C. P. De Mattos, *J. Biomed. Biotechnol.*, 2010, **2010**, 376218.
- 6 J. R. N. McLean, H. C. Birnboim, R. Pontefact and J. G. Kaplan, *Chem.-Biol. Interact.*, 1983, **46**, 189–200.
- 7 T. Şişman, *Environ. Toxicol.*, 2011, **26**, 240–249.
- 8 A. Niknezhadi and A. Nezamzadeh-Ejhieh, *J. Colloid Interface Sci.*, 2017, **501**, 321–329.
- 9 C. H. Lien, C. C. Hu, Y. D. Tsai and D. S. H. Wang, *ECS Trans.*, 2013, **50**, 147–163.
- 10 Y.-D. Tsai, C.-H. Lien and C.-C. Hu, *Electrochim. Acta*, 2011, **56**, 7615–7621.
- 11 P. Ravichandiran, D. S. Prabakaran, N. Maroli, A. R. Kim, B. H. Park, M. K. Han, T. Ramesh, S. Ponpandian and D. J. Yoo, *J. Hazard. Mater.*, 2021, **419**, 126409.
- 12 P. Ravichandiran, D. S. Prabakaran, A. P. Bella, A. Boguszewska-Czubara, M. Maslyk, K. Dineshkumar, P. M. Johnson, B.-H. Park, M.-K. Han, H. G. Kim and D. J. Yoo, *ACS Sustainable Chem. Eng.*, 2020, **8**(29), 10947–10958.
- 13 J. Cheng, E. Yang, P. Ding, J. Tang, D. Zhang, Y. Zhao and Y. Ye, *Sens. Actuators, B*, 2015, **221**, 688–693.
- 14 Q. Wang, C. Li, Y. Zou, H. Wang, T. Yi and C. Huang, *Org. Biomol. Chem.*, 2012, **10**, 6740–6746.
- 15 H. Lan, Y. Wen, Y. Shi, K. Liu, Y. Mao and T. Yi, *Analyst*, 2014, **139**, 5223–5229.
- 16 S. Pu, Y. Xue, C. Zheng, W. Geng, S. Cui and G. Liu, *Tetrahedron*, 2014, **70**, 9070–9076.
- 17 S. Adhikari, S. Mandal, A. Ghosh, S. Guria and D. Das, *Dalton Trans.*, 2015, **44**, 14388–14393.
- 18 P. Ravichandiran, D. S. Prabakaran, N. Maroli, A. Boguszewska-Czubara, M. Maslyk, A. R. Kim, P. Kolandaivel, P. Ramalingam, B. H. Park, M. K. Han, T. Ramesh and D. J. Yoo, *J. Hazard. Mater.*, 2021, **415**, 125593.



19 L. Brulikova, T. Volna and J. Hlavac, *ACS Omega*, 2020, **5**, 9324–9333.

20 X. Meng, L. You, S. Li, Q. Sun, X. Luo, H. He, J. Wang and F. Zhao, *RSC Adv.*, 2020, **10**, 37735–37742.

21 X. Meng, D. Cao, Z. Hu, X. Han, Z. Li and W. Ma, *RSC Adv.*, 2018, **8**, 33947–33951.

22 X. Cheng, S. Qu, L. Xiao, W. Li and P. He, *J. Photochem. Photobiol. A*, 2018, **364**, 503–509.

23 C. G. Chen, N. Vijay, N. Thirumalaivasan, S. Velmathi and S. P. Wu, *Spectrochim. Acta, Part A*, 2019, **219**, 135–140.

24 S. Mukherjee, S. Hazra, S. Chowdhury, S. Sarkar, K. Chattopadhyay and A. Pramanik, *J. Photochem. Photobiol. A*, 2018, **364**, 635–644.

25 K. S. Mani, R. Rajamanikandan, B. Murugesapandian, R. Shankar, G. Sivaraman, M. Ilanchelian and S. P. Rajendran, *Spectrochim. Acta, Part A*, 2019, **214**, 170–176.

26 W. Wang, J. Wu, Q. Liu, Y. Gao, H. Liu and B. Zhao, *Tetrahedron Lett.*, 2018, **59**, 1860–1865.

27 G. Zhu, Y. Huang, C. Wang, L. Lu, T. Sun, M. Wang, Y. Tang, D. Shan, S. Wen and J. Zhu, *Spectrochim. Acta, Part A*, 2019, **210**, 105–110.

28 H. Li, X. Sun, T. Zheng, Z. Xu, Y. Song and X. Gu, *Sens. Actuators, B*, 2019, **279**, 400–409.

29 F. Borges, F. Roleira, N. Milhazes, L. Santana and E. Uriarte, *Curr. Med. Chem.*, 2005, **12**, 887–916.

30 N. Mergu, M. Kim and Y.-A. Son, *Spectrochim. Acta, Part A*, 2018, **188**, 571–580.

31 C. Zhao, J. Chen, D. Cao, J. Wang and W. Ma, *Tetrahedron*, 2019, **75**, 1997–2003.

32 L. I. Li, S. Yun, Z. Yuan-Hui, M. U. Lan, Z. Xi, C. Redshaw and W. E. I. Gang, *Sens. Actuators, B*, 2016, **226**, 279–288.

33 X. Meng, S. Li, W. Ma, J. Wang, Z. Hu and D. Cao, *Dyes Pigm.*, 2018, **154**, 194–198.

34 G. Ambrosi, M. Formica, V. Fusi, L. Giorgi, E. Macedi, G. Piersanti, M. Retini, M. A. Varrese and G. Zappia, *Tetrahedron*, 2012, **68**, 3768–3775.

35 H. Hosseini-Jani-Pirdehi, N. O. Allah Mahmoodi, A. Taheri, K. A. A. Asalemi and R. Esmaeili, *Spectrochim. Acta, Part A*, 2020, **229**, 117989.

36 X. Liu, J. M. Cole and K. S. Low, *J. Phys. Chem. C*, 2013, **117**, 14731–14741.

37 I. H. Hwang, Y. W. Choi, K. B. Kim, G. J. Park, J. J. Lee, L. Nguyen, I. Noh and C. Kim, *New J. Chem.*, 2016, **40**, 171–178.

38 B. Bodenant, F. Fages and M.-H. Delville, *J. Am. Chem. Soc.*, 1998, **120**, 7511–7519.

39 M. A. Lichtman and R. I. Weed, *Blood*, 1969, **34**, 645–660.

40 T. Jiang, L.-C. Tian, C. Huang, B.-X. Zhu, D.-M. Chen and C. Zhu, *Inorg. Chim. Acta*, 2023, **547**, 121367.

41 S. Sharifi, A. Wahid Mesbah and E. Iravani, *Results Chem.*, 2023, **5**, 100747.

42 P. Patil, S. Shinde and S. Sahoo, *Trends Sci.*, 2022, **19**, 4487.

43 J. Li, Y. Chen, T. Chen, J. Qiang, Z. Zhang, T. Wei, W. Zhang, F. Wang and X. Chen, *Sens. Actuators, B*, 2018, **268**, 446–455.

44 L. Guo, X. Chen, R. Xie, L. Han and N. Zhu, *J. Mol. Struct.*, 2023, **1275**, 134615.

45 B. Musikavanhu, D. Zhu, M. Tang, Z. Xue, S. Wang and L. Zhao, *Spectrochim. Acta, Part A*, 2023, **289**, 122242.

46 F. T. Souto and V. G. Machado, *Carbohydr. Polym.*, 2023, **304**, 120480.

47 S. Suguna, R. Nandhakumar and J. Prabhu, *Spectrochim. Acta, Part A*, 2023, **288**, 122196.

48 P. Rasin, J. Haribabu, K. M. Malappuram, V. Manakkadan, V. N. V. Palakkeezhillam, C. Echeverria and A. Sreekanth, *J. Photochem. Photobiol. A*, 2023, **437**, 114493.

49 P. Mohanty, P. P. Dash, S. Naik, R. Behura, M. Mishra, H. Sahoo, S. K. Sahoo, A. K. Barick and B. R. Jali, *J. Photochem. Photobiol. A*, 2023, **437**, 114491.

50 S. Sharma, Chayawan, A. Jayaraman, J. Debnath and K. S. Ghosh, *J. Photochem. Photobiol. A*, 2023, **437**, 114408.

51 M. Abdollahi-Moghadam, H. Keypour, R. Azadbakht and M. Koolivand, *J. Mol. Struct.*, 2023, **1273**, 134289.

52 M. Yu, B. Liu, J. Guo and F. Wu, *Dyes Pigm.*, 2023, **210**, 110983.

53 A. Kumar, B. M. Virender, J. Parikh and K. Modi, *Spectrochim. Acta, Part A*, 2023, **285**, 121889.

54 S. Suguna, A. Puthoor, D. Parimala devi, A. Abiram, R. Nandhakumar and J. Prabhu, *J. Photochem. Photobiol. A*, 2023, **435**, 114268.

55 N. K. Choudhary, L. L. Mittapelli, P. Kumar Roy, G. Das, M. Mandal and K. R. Gore, *Spectrochim. Acta, Part A*, 2023, **285**, 121887.

56 L. J. Gomes, J. P. Carrilho, P. M. Pereira and A. J. Moro, *Sensors*, 2023, **23**, 471.

57 L. K. Shaji, J. Jose, R. Bhaskar, R. Selva Kumar, V. Vetriarasu, S. G. Bhat and S. K. Ashok Kumar, *Inorg. Chem. Commun.*, 2023, **147**, 110252.

58 T. Nantapon, P. Naweephantana, P. Surawatanawong, P. Saetear, T. Chantarojsiri and N. Ruangsupapichat, *Spectrochim. Acta, Part A*, 2022, **282**, 121662.

59 D. Ravichandran, M. Ranjani, G. Prabu Sankar, R. Shankar, M. Karthi, S. Selvakumar and R. Prabhakaran, *J. Mol. Struct.*, 2023, **1273**, 134329.

60 J. M. V. Ngororabanga, T. O. Dembaremba, N. Mama and Z. R. Tshentu, *Spectrochim. Acta, Part A*, 2023, **289**, 122202.

61 R. Gao, X. Liu, J. Feng, L. Han, J. Xu and C. Kan, *Spectrochim. Acta, Part A*, 2022, **281**, 121612.

62 P. Ravichandiran, D. S. Prabakaran, N. Maroli, A. Boguszewska-Czubara, M. Maśłyk, A. R. Kim, P. Kolandaivel, P. Ramalingam, B.-H. Park, M.-K. Han, T. Ramesh and D. J. Yoo, *J. Hazard. Mater.*, 2021, **415**, 125593.

63 P. Ravichandiran, V. K. Kaliannagounder, A. P. Bella, A. Boguszewska-Czubara, M. Maśłyk, C. S. Kim, C. H. Park, P. M. Johnson, B.-H. Park, M.-K. Han, A. R. Kim and D. J. Yoo, *Anal. Chem.*, 2021, **93**, 801–811.

64 Z. Yan, G. Wei, S. Guang, M. Xu, X. Ren, R. Wu, G. Zhao, F. Ke and H. Xu, *Dyes Pigm.*, 2018, **159**, 542–550.

65 V. Singh Rana, V. Anand, S. Shekhar Sarkar, N. Sandhu, M. Verma, S. Naidu, K. Kumar, R. K. Yadav, R. Shrivastava and A. P. Singh, *J. Photochem. Photobiol. A*, 2023, **436**, 114409.



66 M. Rahman and H. J. Harmon, *Spectrochim. Acta, Part A*, 2006, **65**, 901–906.

67 M. Pannipara, A. G. Al-Sehemi, A. Kalam, A. M. Asiri and M. N. Arshad, *Spectrochim. Acta, Part A*, 2017, **183**, 84–89.

68 M. J. Frisch, G. W. Trucks, H. B. Schlegel, G. E. Scuseria, M. A. Robb, J. R. Cheeseman, G. Scalmani, V. Barone, G. A. Petersson, H. Nakatsuji, X. Li, M. Caricato, A. V. Marenich, J. Bloino, B. G. Janesko, R. Gomperts, B. Mennucci, H. P. Hratchian, J. V. Ortiz, A. F. Izmaylov, J. L. Sonnenberg, D. Williams-Young, F. Ding, F. Lipparini, F. Egidi, J. Goings, B. Peng, A. Petrone, T. Henderson, D. Ranasinghe, V. G. Zakrzewski, J. Gao, N. Rega, G. Zheng, W. Liang, M. Hada, M. Ehara, K. Toyota, R. Fukuda, J. Hasegawa, M. Ishida, T. Nakajima, Y. Honda, O. Kitao, H. Nakai, T. Vreven, K. Throssell, J. A. Montgomery Jr, J. E. Peralta, F. Ogliaro, M. J. Bearpark, J. J. Heyd, E. N. Brothers, K. N. Kudin, V. N. Staroverov, T. A. Keith, R. Kobayashi, J. Normand, K. Raghavachari, A. P. Rendell, J. C. Burant, S. S. Iyengar, J. Tomasi, M. Cossi, J. M. Millam, M. Klene, C. Adamo, R. Cammi, J. W. Ochterski, R. L. Martin, K. Morokuma, O. Farkas, J. B. Foresman and D. J. Fox, *Gaussian 09, Revision D.01*, Gaussian, Inc., Wallingford, CT, 2009.

69 J. Tomasi, B. Mennucci and R. Cammi, *Chem. Rev.*, 2005, **105**, 2999–3094.

70 T. Lu and F. Chen, *J. Comput. Chem.*, 2012, **33**, 580–592.

71 W. Humphrey, A. Dalke and K. Schulten, *J. Mol. Graphics*, 1996, **14**(33–38), 27–38.

